

Computer simulations of bilayer membranes: Self-assembly and interfacial tension

Rüdiger Goetz and Reinhard Lipowsky^{a)}

Max-Planck-Institut für Kolloid- und Grenzflächenforschung, Kantstrasse 55, D-14513 Teltow-Seehof, Germany

(Received 30 October 1997; accepted 27 January 1998)

Binary Lennard-Jones fluids consisting of “solvent” and “surfactant” molecules are studied as simplified model systems for amphiphilic molecules in solution. Using Monte Carlo and molecular dynamics simulations, we observe the self-assembly of the surfactant molecules into bilayer membranes. These bilayers are fluid since the surfactants exhibit rapid lateral diffusion. We also measure the interfacial tension and the compressibility modulus of these bilayers. We show that they exhibit a *tensionless* state and characterize the corresponding stress profile. In this way, we bridge the gap between previous theoretical studies which were based (i) on discrete models with atomic resolution and (ii) on continuum models in which the bilayer membrane is treated as a smooth surface. © 1998 American Institute of Physics. [S0021-9606(98)50717-9]

I. INTRODUCTION

Solutions of amphiphilic molecules such as lipids in water are characterized by a wide range of length scales. These molecules usually resemble semiflexible rods with a length of the order of 1–2 nm, which is already large compared to the atomic size ≈ 0.1 nm. In solution, these rodlike molecules form supramolecular aggregates such as spherical and cylindrical micelles or bilayers. Spherical micelles have a diameter which is roughly twice the length of the amphiphiles. The thickness of cylindrical micelles is of the same order but their longitudinal extension is usually much larger. Likewise, the thickness of bilayers is again about twice the rod length, i.e., 2–4 nm but their lateral extension can be many micrometers.

Previous theoretical work on bilayer membranes has been done on two different types of models. On the one hand, coarse-grained surface models for these membranes have been studied in which the membranes are treated as smooth and continuous surfaces; for recent reviews, see Ref. 1. In these studies, one focuses on the membrane behavior on length scales which are large compared to the membrane thickness. Thus, in these continuum models, the bilayer thickness is treated as a small-scale cutoff and the molecular structure of the bilayer is not taken into account explicitly.

On the other hand, bilayer models with (almost) atomic resolution have been studied by extensive computer simulations; see, e.g., Refs. 2–5. Since these simulations require a huge amount of computing time, they are restricted to relatively small bilayer segments which contain 50–200 amphiphilic molecules. For a lipid bilayer, this corresponds to a membrane area of the order of $(3 \text{ nm})^2$ – $(8 \text{ nm})^2$.

The main goal of the present paper is to bridge the gap between these two types of models, i.e., between discrete models with atomic resolution on the one side and continuum surface models on the other side. In order to do this,

we will study effective molecular models which describe the membrane behavior on *intermediate* length scales, see Sec. II. Our models are binary Lennard-Jones fluids consisting of “solvent” and “surfactant” molecules. The surfactant consists of a head group and one or two tails which are modeled by chains of particles interconnected by a harmonic bond potential. In addition, we incorporate the bending stiffness of these chains.

Since we do not attempt to incorporate all details on the atomic or molecular level, we are able to simulate *different* cooperative phenomena in the *same* model system. These different phenomena include the formation of self-assembled aggregates, see Sec. III, the fluidity of bilayers characterized by rapid lateral diffusion but very rare transverse diffusion (or flip-flop), see Sec. IV; and the interfacial tension and the area compressibility of bilayer membranes, see Sec. V. Thus, within these simplified model systems, *both* the self-assembly process of the bilayer *and* the bilayer properties are accessible within the same type of simulation. In contrast, previous simulation studies have focused *either* on the self-assembly process of the amphiphiles which was usually investigated by Monte Carlo (MC) simulations *or* on the physical properties of preassembled bilayers as observed via molecular dynamics (MD) simulations.

Our model systems are characterized by a relatively *small* number of parameters. Therefore, we can systematically vary these parameters and then study how the different cooperative phenomena are affected by this variation. Two important parameters are the size and the tail flexibility of the surfactants. Thus, in the present study, we will consider three different types of model surfactants which differ in their size and their tail flexibility and compare their cooperative behavior.

In general, surfactant molecules are characterized, for a given solvent, by two different segments: a soluble or lyophilic segment and an insoluble or lyophobic segment. In the models studied here, this difference in solubility is described

^{a)} Author to whom correspondence should be addressed.

by two different pair interactions which act (i) between the solvent and the lyophilic segment of the surfactant and (ii) between the solvent and the lyophobic segment. This difference in the pair interactions drives the self-assembly of the molecules into micelles and bilayers as described below. Similar models have been previously studied for ternary mixtures of oil, water, and surfactant.⁶⁻¹⁰ A lattice model for binary systems has been recently studied by MC simulations.¹¹

For surfactant molecules in aqueous solution, the self-assembly is believed to be primarily driven by *entropic* contributions which arise from the fluctuating network of hydrogen bonds within the water.¹² In this case, the effective pair interactions used in our models have an entropic component and will, thus, depend on temperature. In the present study, we do not address this dependence since all our model systems are taken to be at the same fixed temperature.

A conceptually simpler situation occurs for surfactant molecules in nonpolar solvents. For such systems, the self-assembly process is believed to be primarily *enthalpic* in origin. One example is provided by solutions of semifluorinated alkanes in hydrocarbons^{13,14} or fluorocarbons^{15,16} for which micellelike aggregates have been observed. In the latter case, the effective interactions between the solvent and the two different surfactant segments should be essentially independent of temperature.

In the following, we will use the terminology which is appropriate to aqueous solutions. In this case, the lyophilic and lyophobic segments are hydrophilic and hydrophobic, respectively. One should keep in mind, however, that our models also apply, in a rather direct way, to surfactant molecules in nonpolar solvents.

II. DEFINITION OF MODEL SYSTEMS

Our model system is built up from three types of “particles” which can be hydrophilic or hydrophobic. Each of these particles represents a group of real atoms, e.g., the surfactant head group, a water molecule, or some CH₂ groups. The three types of particles are hydrophilic solvent particles, i.e., water particles, hydrophilic surfactant-head group particles, and hydrophobic tail particles for the tails of the surfactants.

We consider N such particles in a stretched simulation box with box width L_{\parallel} and box height L_{\perp} . The volume of the simulation box is given by $L_{\parallel}^2 L_{\perp}$ and the overall particle number density by $n = N / (L_{\parallel}^2 L_{\perp})$. For simplicity, all particles are taken to be spherical balls and to have the same mass m . The positions of the particle i at time t is given by the vector $\mathbf{r}_i = \mathbf{r}_i(t)$, which points to the center of mass of the particle. The relative position of two particles at $\mathbf{r} = \mathbf{r}_i$ and $\mathbf{r} = \mathbf{r}_j$ is given by the vector $\mathbf{r}_{ij} = \mathbf{r}_j - \mathbf{r}_i$; the distance between these two particles by $r_{ij} = |\mathbf{r}_{ij}|$.

A. Interaction potentials

The interactions between one hydrophilic and one hydrophobic particle is modeled by a repulsive soft core potential as given by

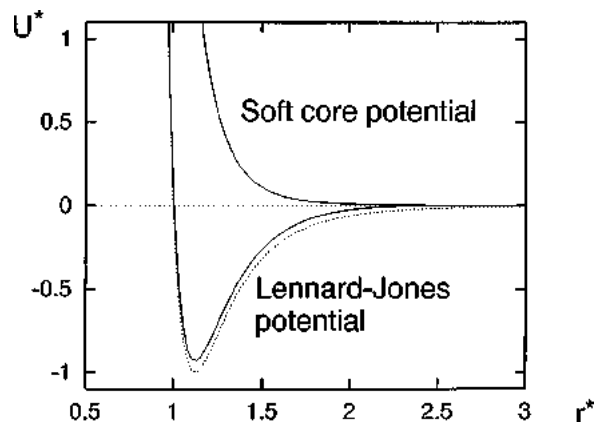


FIG. 1. The interparticle potentials U^* as a function of the dimensionless distance r^* : The lower and upper full curves correspond to the shifted force Lennard-Jones potential and to the shifted force soft core potential, respectively. For comparison, the unshifted Lennard-Jones potential is also shown as the dotted line.

$$U_{SC}(r) \equiv 4 \epsilon \left(\frac{\sigma_{SC}}{r} \right)^9. \quad (2.1)$$

All other interactions are modeled by an attractive Lennard-Jones potential of the form

$$U_{LJ}(r) \equiv 4 \epsilon \left[\left(\frac{\sigma}{r} \right)^{12} - \left(\frac{\sigma}{r} \right)^6 \right]. \quad (2.2)$$

These interparticle potentials are shown in Fig. 1. Note that the minimal value of U_{LJ} is given by $-\epsilon$.

For simplicity, we take all potential energy functions to have the same cutoff radius $r_c = 2.5\sigma$. Likewise the energy and length scales are taken to be the same for all pairs of particles. The parameter σ_{SC} was chosen to be $\sigma_{SC} = 1.05\sigma$; for this choice, the hard-core repulsion of the soft core potential is approximately as strong as the repulsive part of the Lennard-Jones potential.

In order to avoid discontinuities in the potential energy and in the force we use the shifted force variant of the potentials, as given by

$$\tilde{U}_X(r) \equiv U_X(r) - U_X(r_c) - \left. \frac{\partial U_X}{\partial r} \right|_{r=r_c} (r - r_c) \quad (2.3)$$

with $U_X = U_{LJ}$ or U_{SC} .

In our model, head group and tail particles are connected by a harmonic bond potential

$$U_2(r_{i,i+1}) = k_2 (|\mathbf{r}_{i,i+1}| - \sigma)^2 \quad (2.4)$$

to form surfactant molecules. The vector $\mathbf{r}_{i,i+1}$ denotes the relative position vector between two neighboring particles along the surfactant chain, see Fig. 2.

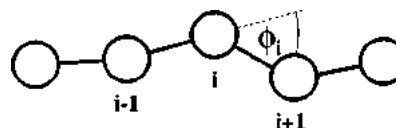


FIG. 2. Geometry of the surfactant chain with tilt angle ϕ_i between two neighboring bonds.

As discussed in Ref. 9, the bond stretching modulus k_2 should be chosen in such a way that only up to 2% of all bonds differ in length by more than 2% from the average bond length σ . It turns out, however, that the simulations are not very sensitive to the value of k_2 as long as k_2 is of the order of $10^3 \cdot \epsilon \sigma^{-2}$. In our simulations, we set $k_2 = 5000 \epsilon \sigma^{-2}$. In this case, up to 10% of the bonds of a given configuration differ by more than 2% from the long time average bond length which is equal to σ . Nevertheless, the average bond length $\langle |r_{i,i+1}| \rangle$ in any configuration differs only up to 0.1% from its long time average σ .

For some of the simulations, we extend the model toward semiflexible surfactant molecules by adding a bending potential along the chains of these molecules. This three-body bending potential is taken to be

$$U_3(\mathbf{r}_{i-1,i}, \mathbf{r}_{i,i+1}) = k_3 \left(1 - \frac{\mathbf{r}_{i-1,i} \cdot \mathbf{r}_{i,i+1}}{|\mathbf{r}_{i-1,i}| |\mathbf{r}_{i,i+1}|} \right) \equiv k_3 (1 - \cos \phi_i), \quad (2.5)$$

where k_3 is the bending modulus of the semiflexible tails and the second equality defines the tilt angle ϕ_i between two neighboring bonds. At temperature T , the persistence length L_p of such a semiflexible chain is then given by¹⁷ $L_p = k_3 \sigma / k_B T$ with the Boltzmann constant k_B . Assuming that the persistence length is of the order of the tail length, one gets a value of $k_3 = 5.4 \epsilon$. In the simulations, we use either $k_3 = 5 \epsilon$ or $k_3 = 2 \epsilon$. The bending potential as given by Eq. (2.5) applies to all particles in the surfactant chain except for the particles at the chain ends.

For more complex surfactants, a spontaneous or preferred tilt angle ϕ_i^{sp} was added to the bending potential which then has the form

$$U_3 = k_3 [1 - \cos(\phi_i - \phi_i^{\text{sp}})] = k_3 [1 - (\cos \phi_i \cos \phi_i^{\text{sp}} + \sin \phi_i \sin \phi_i^{\text{sp}})]. \quad (2.6)$$

The potential energy Φ of the whole system is then given by

$$\Phi(\{\mathbf{r}_i\}) = \sum_{\langle ij \rangle} \tilde{U}_X(r_{ij}) + \sum_c \sum_i U_2(r_{i,i+1}) + \sum_c \sum_i U_3(\mathbf{r}_{i,i-1}, \mathbf{r}_{i,i+1}), \quad (2.7)$$

where $\langle ij \rangle$ and c indicate a summation over all particle pairs and over all chains, respectively. The summation over i includes all contributions for a given chain c ; if the chain contains n_c particles, it contributes $(n_c - 1) U_2$ terms and $(n_c - 2) U_3$ terms.

B. Different surfactant molecules

In general, we can investigate many different model surfactants which differ in their geometry and their chain flexibility. In the present work, we focus on three different surfactants. In order to distinguish these molecules, we will denote the water particles by w , the head group particles by h , and the tail particles by t . Capital letters indicate that the chains are semiflexible. The three types of surfactants are denoted as (see Fig. 3):

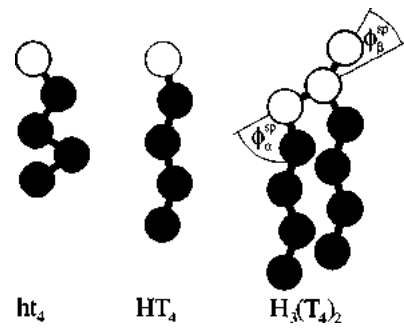


FIG. 3. Three types of surfactants used in this study. The white particles [(h) or (H)] represent the head group, the black particles [(t) or (T)] the tail.

- (i) ht_4 surfactants with one head group particle and four tail particles. The surfactant tails are flexible;
- (ii) HT_4 surfactants as in (i) but with semiflexible tails; and
- (iii) $H_3(T_4)_2$ surfactants. These surfactants with two tails are taken as a crude model for lipid molecules. For these molecules, the preferred bond angle ϕ_i is set to zero except for the two angles displayed in Fig. 3. The values of the preferred bond angle are taken to be $\phi_\alpha^{\text{sp}} = 5\pi/12$ and $\phi_\beta^{\text{sp}} = \pi/6$, which leads to head groups reminiscent of typical lipid molecules.

The simulation data described below were obtained using a recently developed code.¹⁸ All simulations were performed in a stretched cubic simulation box. As mentioned, we denote the box width by L_{\parallel} and the box height by L_{\perp} . The overall particle density n was set to $n = 2/3 \sigma^3$ in all simulations. Periodic boundary conditions are applied in all three directions. Additional technical details are given in Appendix A.

C. Dimensionless quantities

In standard MD simulations, the fundamental scales of mass (m), length (σ), and energy (ϵ) give well-defined scales for all measurable quantities. The time scale, for example, is given by $t_{\text{sc}} = \sqrt{m \sigma^2 / \epsilon}$.

In the following, we will denote dimensionless quantities by an asterisk, such as, e.g., the dimensionless area $A^* \equiv A / \sigma^2$. There is one exception to this rule: The dimensionless time t^* is defined via $t^* \equiv t / \Delta t$ where $\Delta t = t_{\text{sc}} / 2000$ is the size of the discrete time step, see Appendix A.

Because we do not associate particles directly with real atoms in our simulation, we have some freedom in the interpretation of measurable quantities. In previous simulations with atomic resolution, the Lennard-Jones length σ was chosen in such a way that a chain segment of length $\approx \sigma$ contained three to four CH_2 groups. In our model, the Lennard-Jones length is chosen to be identical with the bond length, i.e., with the distance between nearest-neighbor particles along the chain. Therefore, one tail particle in our model corresponds to three to four CH_2 groups.

This correspondence implies that the mass of one particle in our simulation lies between the mass of one water molecule and the mass of four CH_2 groups, i.e., 18 g/mol

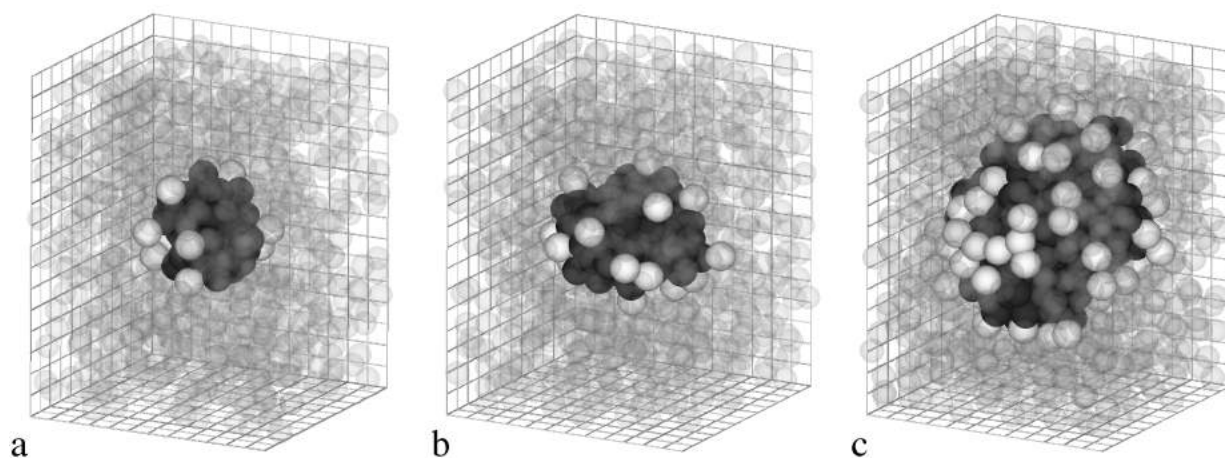


FIG. 4. Micellar aggregates formed by flexible ht_4 surfactants: (a) Spherical micelle containing 10 flexible ht_4 surfactants ($c_s=0.035$). (b) Spherical micelle containing 20 flexible ht_4 surfactants ($c_s=0.069$). (c) Spherical micelle containing 60 flexible ht_4 surfactants ($c_s=0.208$). The black, white, and translucent beads represent the tail, head group, and water particles, respectively.

$\leq N_{Av}m \leq 56$ g/mol where N_{Av} denotes the Avogadro number. Likewise, we take the Lennard-Jones length σ and energy ϵ to be of the same order as in Ref. 2 for pairs of CH_2 groups and/or CH_3 groups and/or water molecules, which implies $0.31 \text{ nm} \leq \sigma \leq 0.374 \text{ nm}$ and $0.42 \text{ kJ mol}^{-1} \leq N_{Av}\epsilon \leq 1.20 \text{ kJ mol}^{-1}$.

In the following we will use the values $\sigma=1/3 \text{ nm}$, $N_{Av}\epsilon=2 \text{ kJ/mol}$, and $N_{Av}m=36 \text{ g/mol}$ for the translation of our results into dimensionful quantities. Our choice $N_{Av}\epsilon=2 \text{ kJ/mol}$ for the energy scale exceeds the values used in Ref. 2 since our particles represent molecular groups which exceed the CH_2 groups in Ref. 2. The energy scale $N_{Av}\epsilon=2 \text{ kJ/mol}$ is equivalent to 324 K or about 50 °C. With this choice for m , ϵ , and σ , we obtain the time scale $t_{sc}=1.4 \text{ ps}$ and simulation times of up to 5 μs . If we made other choices which are consistent with the above parameter intervals, the time scale t_{sc} could vary by a factor of 4.

III. SELF-ASSEMBLY OF MODEL SURFACTANTS

First, we study the self-assembly behavior of our model surfactants by performing several simulations at different surfactant concentrations for all three types of surfactant molecules. As initial configurations, we used uniform random distributions of water and surfactant molecules.

The surfactant concentration is defined by

$$c_s \equiv (N_t + N_h)/N, \quad (3.1)$$

where N_t , N_h , and N are the number of tail particles, head group particles, and the total number of particles (including water particles), respectively. The same series of concentrations is used for both the ht_4 and the HT_4 surfactants. For the systems with $H_3(T_4)_2$ surfactants, the number of surfactant molecules was chosen in such a way that the resulting concentrations closely match those of ht_4 .

First, we report results for a simulation box with $L_{\parallel}=12\sigma$ and $L_{\perp}=15\sigma$. This choice of the simulation box corresponds to the typical size used in Sec. IV where we study the stretching elasticity.

During the initial MC simulation, the surfactants start to aggregate and form small micellelike structures containing up to ten surfactant molecules. In the subsequent MD simulations, these small aggregates merge into larger micelles. At low surfactant concentration, this process leads to one large spherical micelle containing all surfactants. Even for a relatively small number N_s of surfactants, i.e., for N_s of the order of 10–15, the resulting micelles are almost spherical, as shown in Fig. 4. For aggregates with only five surfactants, this still applies to the average shape but no longer to a typical configuration as seen in a snapshot.

Because of the periodic boundary conditions, a large micelle merges with itself at high concentrations in one or two directions and forms either an infinite long cylindrical micelle or a bilayer, see Fig. 5.

For most aggregates, the assembly process takes between 1 and 5×10^5 time steps. These times decrease first with increasing surfactant concentration but then increase again, see Table I. This is due to a process of internal rearrangement of the surfactants in the large aggregates. Furthermore, the merging process at high concentrations takes some time as well. At very low concentrations, small micellelike aggregates move sometimes almost parallel through the simulation box and do not fuse for relatively long times. In the latter case, the aggregation times are much larger.

A crude estimate of the surface and the volume of the aggregates may be obtained by fitting a sphere or a cylinder to the end configurations of these micellar aggregates. Dividing by the number of surfactants, one gets the surface area and volume per surfactant molecule as given in Table I.

The surface area per surfactant molecule decreases with increasing size of the aggregates, while the volume per surfactant stays almost constant. This agrees with the volume incompressibility of surfactants as observed in real systems.

The results for HT_4 surfactants are similar to those for ht_4 apart from the high concentration regime, see Table I. Here we found a vertically oriented bilayer containing a pore. By direct observation of the corresponding assembly

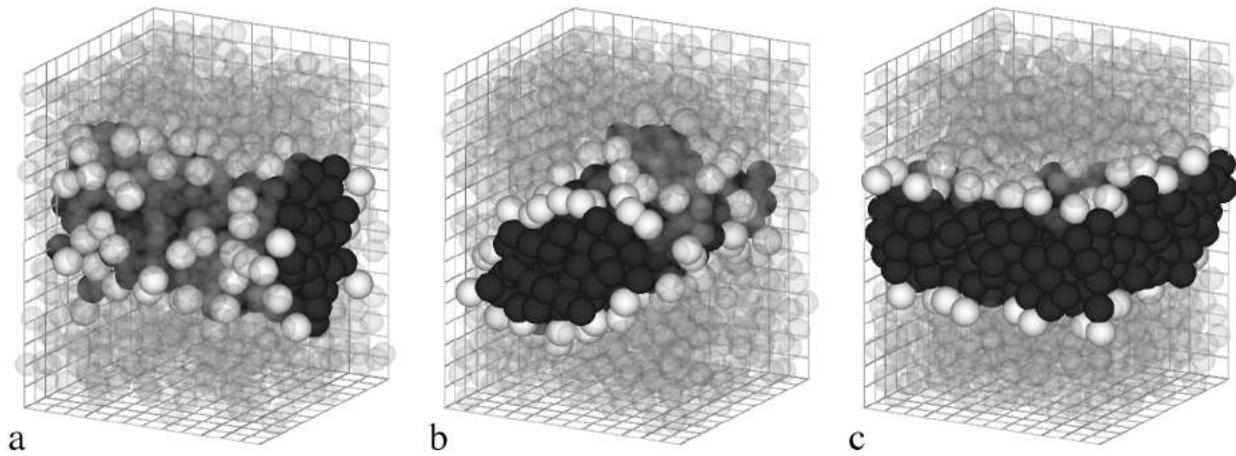


FIG. 5. Aggregates formed by flexible ht_4 surfactants: (a) Cylindrical micelle containing 80 flexible ht_4 surfactants ($c_s=0.278$), (b) flattened cylindrical micelle containing 80 flexible ht_4 surfactants ($c_s=0.347$), and (c) bilayer containing 110 flexible ht_4 surfactants ($c_s=0.382$). The beads are colored in the same way as in Fig. 4.

process, one finds that, in the high concentration regime, the merging of the small micellar structures occurs at two centers. Because of the box geometry, one of those centers is located in the upper part of the box and the other in the lower part. These two micelles prefer to merge to one vertically oriented object rather than to an horizontally oriented one.

For the parameter values, for which the surfactants form a vertical bilayer with a pore, these molecules could also form a horizontal bilayer without such a pore. In fact, the vertical pore state should have a free energy which exceeds the one for the horizontal state since (i) the vertical state is stretched more strongly than the horizontal one (i.e., the pore does not relax all the stress in the vertical bilayer) and (ii) the pore has an edge tension which gives an additional contribution to the free energy of the vertical state. Therefore, the vertical pore state should represent a metastable state and should relax toward the horizontal state on sufficiently long time scales. However, we found no such relaxation process in 1.5×10^6 time steps. This implies that the vertical pore

state is kinetically trapped because of the large activation barrier associated with the disassembly of the vertical bilayer.

Self-assembly of the $H_3(T_4)_2$ surfactants leads to similar aggregates, see Table II. Cylindrical micelles occur at somewhat lower concentrations $c_s \approx 0.2$ and no bilayers are found at high concentration for this choice of the box size. However, a bilayer containing 55 $H_3(T_4)_2$ surfactants would have the area $A_s = 5.5\sigma^2$ per surfactants. This is a lot bigger than the value obtained for a stress free bilayer, see Sec. IV. Therefore, a cylindrical micelle is formed instead of a bilayer under high stress.

In order to check if bilayer formation is also possible for HT_4 or $H_3(T_4)_2$ surfactants, we performed additional simulations in a more elongated simulation box with $L_{\parallel} = 10\sigma$ and $L_{\perp} = 21.6\sigma$ for $H_3(T_4)_2$ and with $L_{\parallel} = 10.5\sigma$ and $L_{\perp} = 19.6\sigma$ for HT_4 . For these box sizes, a nice horizontal bilayer was found for the surfactant concentration $c_s = 0.42$ for both types of surfactants.

TABLE I. Aggregates of N_s surfactants with one tail corresponding to surfactant concentration c_s : (left) Flexible ht_4 surfactants and (right) semiflexible HT_4 surfactants with bending modulus $k_3 = 2\epsilon$. The assembly times t_{as} are given in units of $10^5 \Delta t$. These times include 10^5 initial MC steps. For the ht_4 surfactants, the volumes V_s^* and the projected surfaces A_s^* per surfactant molecule are also displayed. For the bilayer state, the projected surface area is given by the cross sectional area of the simulation box divided by the number of molecules. Hence there is no error in this estimate.

N_s	c_s	ht_4 surfactants				HT_4 surfactants	
		Aggregate type	t_{as}	V_s^*	A_s^*	Aggregate type	T_{as}
5	0.017	Sph. micelle	290	8.9 ± 4.2	12.2 ± 3.5	Sph. micelle	230
10	0.035	Sph. micelle	950	9.2 ± 3.8	9.9 ± 2.6	Sph. micelle	250
20	0.069	Sph. micelle	550	9.0 ± 2.9	7.7 ± 1.6	Sph. micelle	740
40	0.139	Sph. micelle	160	9.2 ± 2.2	6.2 ± 1.0	Sph. micelle	330
60	0.208	Sph. micelle	220	8.7 ± 2.2	5.2 ± 0.9	Sph. micelle	140
80	0.278	Cyl. micelle	240	8.2 ± 1.8	3.9 ± 0.4	Cyl. micelle	200
100	0.347	Flat. cyl. micelle	380	8.6 ± 1.5	3.8 ± 0.3	Flat. cyl. micelle	160
110	0.382	Horizontal bilayer	540	8.8 ± 0.9	2.4 ± 0.0		
120	0.417					Vertical bilayer with a pore	200

TABLE II. Aggregates of N_S semiflexible $H_3(T_4)_2$ surfactants with two tails and bending modulus $k_3 = 2\epsilon$ corresponding to surfactant concentration c_s . The units for the assembly time t_{as} are the same as given in Table I.

N_S	c_s	Aggregate type	t_{as}
5	0.038	Sph. micelle	750
9	0.069	Sph. micelle	600
15	0.115	Sph. micelle	1110
18	0.138	Sph. micelle	310
27	0.208	Cyl. micelle	200
55	0.420	Cyl. micelle	1000

In conclusion, we found that all three types of surfactant were capable of forming spherical micelles, cylindrical micelles, and bilayers. Because of the periodic boundary conditions, the bilayer state corresponds to a lamellar state for which the separation of the bilayers is equal to L_\perp .

IV. MOBILITY OF WATER AND SURFACTANT

The next thing to check is whether the self-assembled bilayers are in a fluid state. This has been done by measuring the rms displacement of the surfactant molecules. For times which exceed about 2×10^5 time steps, this quantity is proportional to \sqrt{t} . This is typical for diffusive motion. Because of the periodic boundary conditions the center of mass of the whole system moves as well. Since all particles have the same mass, the center-of-mass coordinate is simply given by $\mathbf{R}(t) = (1/N) \sum_i \mathbf{r}_i(t)$ where the sum over i includes all particles. The particle displacements relative to this overall motion are defined via $\Delta \mathbf{r}_i(t) = \mathbf{r}_i(t) - \mathbf{R}(t)$. One can then define a time-dependent diffusion coefficient $D(t)$ via

$$D(t) \equiv \frac{\sum_i [\Delta \mathbf{r}_i(t) - \Delta \mathbf{r}_i(0)]^2}{6Nt}. \quad (4.1)$$

For long t , this diffusion coefficient approaches the asymptotic mean value \bar{D} , see Fig. 6.

As mentioned before, because of the periodic boundary conditions, the bilayer segment spanning the simulation box corresponds to a lamellar state of bilayers. Therefore one has to distinguish the lateral and the transverse diffusive motions, which are governed by two different diffusion coefficients D_\parallel and D_\perp . The diffusion coefficient D_\parallel is defined by

$$D_\parallel(t) \equiv \frac{\sum_i [\Delta \mathbf{r}_{\parallel i}(t) - \Delta \mathbf{r}_{\parallel i}(0)]^2}{6Nt}, \quad (4.2)$$

where $\Delta \mathbf{r}_{\parallel i}(t)$ is the lateral component of $\Delta \mathbf{r}_i(t)$. D_\parallel is also displayed in Fig. 6.

Inspection of Fig. 6 shows that, for the surfactant molecules, the asymptotic mean value \bar{D}_\parallel of $D_\parallel(t)$ for large t is found to be essentially equal to \bar{D} . By following the paths of some tracer molecule in the bilayer, one can directly observe that the surfactant molecules exchange their position within the bilayer. The rapid diffusion measured along the bilayer shows that this surfactant bilayer is in a fluid phase.

In addition to the lateral diffusion of the surfactant molecules, we also observed transmembrane diffusion or flip-

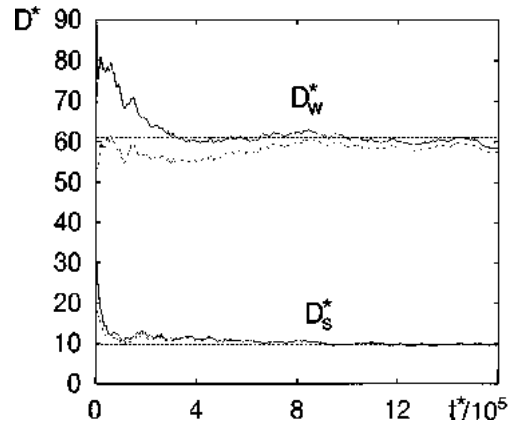


FIG. 6. The time evolution of the reduced diffusion coefficient $D^* \equiv Dt_{sc}/\sigma^2 = D\sqrt{m}/(\sigma^2\epsilon)$. For large time t , the diffusion coefficients D^*_w and D^*_s for water and for surfactant particles attains asymptotic mean values \bar{D}^*_w and \bar{D}^*_s corresponding to the straight dashed lines. The dashed-dotted curves correspond to the lateral diffusion coefficients D_\parallel , as defined in Eq. (4.2)

flops of surfactant molecules, but only very rarely.¹⁸ A more detailed discussion of the observed flip-flop process will follow in a forthcoming paper.

As shown in Fig. 6, the asymptotic mean value \bar{D}_\parallel of the lateral diffusion coefficient for the water particles is close to the asymptotic mean value \bar{D} of the total diffusion coefficient but shows a small systematic deviation from \bar{D} . The difference $\bar{D} - \bar{D}_\parallel$ arises from the finite permeability of the bilayer membrane for water molecules.

The measured values of the diffusion coefficients \bar{D}_w and \bar{D}_s for the water and the surfactant particles, respectively, are displayed in Table III.

V. INTERFACIAL TENSION AND STRESS PROFILE

Real bilayers in solution often attain a state which is essentially tensionless and which then has interesting elastic properties. As will be shown in Sec. VI, it takes a certain effort to obtain such states in computer simulations. Indeed, the bilayer segments which can be studied via simulations are constrained by boundary conditions which usually induce substantial interfacial tensions.

In order to attain an essentially tensionless state of the bilayer membrane in simulations, one has to determine the projected tension as a function of the size of the simulation box for fixed surfactant number. The size of the simulation box determines the projected area A_s per surfactant molecule via $A_s = L_\parallel^2/N_s$. Close to the tensionless state with $A_s = A_{s0}$ the stretching free energy F_s behaves as $F_s \approx K_A [(A_s - A_{s0})/A_{s0}]^2$ with the area compressibility modulus K_A as follows from the classical elasticity theory for elastic sheets. The interfacial tension is the derivative of F_s with respect to the relative area change $\delta A = (A_s - A_{s0})/A_{s0}$ and thus given by $\Sigma = \partial F_s / \partial \delta A \approx K_A (A_s - A_{s0})/A_{s0}$. Thus, in order to study the state of the bilayers, we have to determine both the projected surfactant area A_s and the interfacial tension Σ . The projected area A_s follows directly via $A_s = L_\parallel^2/N_s$. The

TABLE III. The diffusion coefficients \bar{D}_W and \bar{D}_S for water and surfactant. The two columns for HT_4 are distinguished by two different values of the bending modulus k_3 . The data were obtained from the last 1.6×10^6 time steps [2.4×10^6 time steps in the case of $H_3(T_4)_2$] of the simulations described in Sec. V. The bilayers are almost tensionless.

Surfactant	ht_4	HT_4	HT_4	$H_3(T_4)_2$
k_3 (ϵ)	0	2	5	2
A_s (σ^2)	2.33	2.14	1.89	4.20
\bar{D}_W ($10^{-6} \cdot \sigma \sqrt{\epsilon m^{-1}}$)	61 ± 2	64 ± 2	62 ± 4	64 ± 3
\bar{D}_W ($10^{-12} \cdot m s^{-2}$)	4.8 ± 0.1	5.0 ± 0.1	4.9 ± 0.3	5.0 ± 0.2
\bar{D}_S ($10^{-6} \cdot \sigma \sqrt{\epsilon m^{-1}}$)	9.6 ± 0.7	9.9 ± 0.5	8.0 ± 1.0	3.6 ± 0.4
\bar{D}_S ($10^{-12} \cdot m s^{-2}$)	0.75 ± 0.05	0.78 ± 0.04	0.63 ± 0.08	0.28 ± 0.03

interfacial tension Σ , on the other hand, requires some non-trivial computations.

A. Macroscopic stress tensor

For a fluid system which is translationally invariant in the lateral directions, parallel to the bilayer, the stress tensor $\Sigma^{\alpha\beta}$ has only two distinct diagonal components, the tangential stress Σ_T and the normal stress Σ_N :

$$\Sigma^{\alpha\beta} = \begin{pmatrix} \Sigma_T & 0 & 0 \\ 0 & \Sigma_T & 0 \\ 0 & 0 & \Sigma_N \end{pmatrix}, \quad (5.1)$$

where the z axis is taken to be normal to the bilayer plane.

Since the system is translationally invariant in the lateral directions, the components of the stress tensor depend only on the coordinate z . Using the mechanical definition of the interfacial tension Σ , one finds¹⁹

$$\Sigma = \int_{-\infty}^{\infty} dz [\Sigma_T(z) - \Sigma_N(z)]. \quad (5.2)$$

The z -dependent function in the integrand represents the stress profile

$$s(z) \equiv \Sigma_T(z) - \Sigma_N(z) \quad (5.3)$$

across the bilayer.

B. Microscopic stress tensor

The macroscopic stress tensor $\Sigma^{\alpha\beta}$ can be expressed in terms of the microscopic stress tensor $\sigma^{\alpha\beta}$, which depends on the positions and momenta of the particles within a small volume V around an arbitrary but fixed position. The tensor $\sigma^{\alpha\beta}$ has a kinetic part and an interaction part. The kinetic part of $\sigma^{\alpha\beta}$ does not contribute to the stress profile $s(z)$ as defined by Eq. (5.3). Explicit expressions for the interaction part $\sigma_{in}^{\alpha\beta}$ are derived in Appendix B. This derivation represents an extension of the work by Schofield and Henderson,²⁰ see also Refs. 21 and 19. The interaction part of the macroscopic stress tensor $\Sigma^{\alpha\beta}$ is then given by

$$\Sigma_{in}^{\alpha\beta} = \langle \sigma_{in}^{\alpha\beta} \rangle, \quad (5.4)$$

where the brackets represent a thermal average.

VI. SIMULATION RESULTS FOR THE INTERFACIAL TENSION

In order to check the reliability of our program, we first performed some simulations with ‘‘pure’’ water, i.e., for a one-component Lennard-Jones fluid, and found a vanishing interfacial tension. Likewise, the off-diagonal components were found to vanish both for pure water and in the presence of a bilayer.

In order to obtain the dependence of the interfacial tension on the stretching of the bilayer, i.e., on the area per surfactant molecule, we performed a series of simulations with varying box width L_{\parallel} but constant number of surfactant molecules $N_S=128$, constant total number of particles $N=1440$, and constant overall density $n=N/V=2/3\sigma^3$. The volume was fixed at $L_{\parallel}^2 L_{\perp} = 2160\sigma^3$. The initial configurations were preassembled bilayers. These initial configurations were relaxed via 1.6×10^5 MC steps and 8×10^5 MD steps.

The interfacial tension of bilayer membranes has been previously studied by MD simulations for models with atomic resolution.²² In this latter work, relatively small systems with 72 phospholipid molecules and 2511 water molecules have been investigated. For these systems, the tension was determined for four values of the surfactant area A_s but no attempt was made to attain states with vanishing tension. In contrast, we have systematically studied bilayer states with small negative or positive tensions and have, thus, been able to interpolate toward tensionless states.

The first measurements of the interfacial tension were done with a sampling interval of 1000 time steps. A careful analysis of the time evolution of the interfacial tension for a short run consisting of 10^4 time steps revealed that, for small systems sizes as used here, the fluctuations of the interfacial tension are about 10 times larger than its average value. Similar tension fluctuations have also been observed in Ref. 22.

In order to reduce these effects of the short time fluctuations, we preaverage the interfacial tensions over 5000 time steps instead of taking only one sample out of this interval. This average value is then used as the sample for this interval. Since the number of samples has not been enlarged, we can still get a reliable estimate of the statistical error.

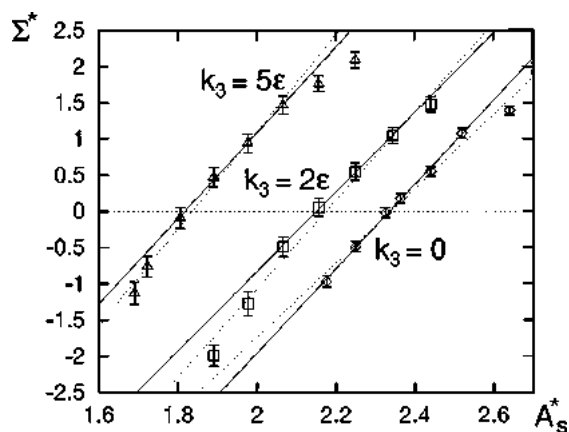


FIG. 7. Functional dependence of the surface tension Σ^* on the area A_s^* per surfactant molecule for flexible ht_4 with bending modulus $k_3=0$ and for semiflexible HT_4 surfactants with $k_3=2\epsilon$ and $k_3=5\epsilon$. The straight lines are linear fits. The dotted lines are alternative fits to estimate the error.

A. Small tension regime

By varying the box width L_{\parallel} , we induced different interfacial tensions on the bilayer. The initial configurations were equilibrated using 6×10^4 MC steps and 8×10^5 MD steps. We then performed a total number of 2.4×10^6 MD steps which were used to calculate thermal averages. After 8×10^5 and 1.6×10^6 MD steps, we inserted intermediate sequences consisting of 5×10^4 MC and 5×10^4 MD steps in order to reach regions of phase space not easily accessible by a single deterministic MD trajectory and thus to enhance the quality of our averages.

Figure 7 shows the results for the flexible ht_4 surfactants and for the semiflexible HT_4 surfactants with two different chain stiffnesses; the inset in Fig. 8 displays the results for the semiflexible two-chain surfactants [$H_3(T_4)_2$].

By fitting a linear function to these data, we determined the area compressibility modulus K_A and the area A_0 per surfactant molecule for the tensionless bilayer. The values of these quantities are given in Table IV. One finds that the area

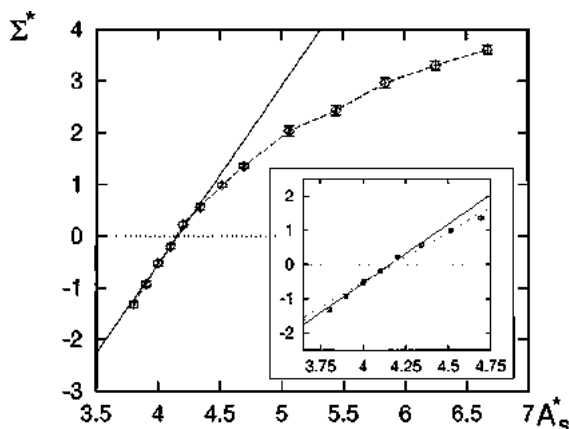


FIG. 8. Surface tension Σ^* as a function of the surfactant area A_s^* for semiflexible two-chain $H_3(T_4)_2$ surfactants. The nonlinear behavior for large A_s^* corresponds to highly stretched bilayers. An enlarged plot of the linear part for small Σ^* is shown in the inset. In this inset, the straight line represents a linear fit; the dotted line is used to estimate the error.

TABLE IV. Area A_{s0} per surfactant molecule and area compressibility modulus K_A for tensionless bilayers. The dimensional quantities in the last two columns were obtained using $\sigma=1/3$ nm, $N_{Av}\epsilon=2$ kJ mol $^{-1}$, and $N_{Av}m=36$ g mol $^{-1}$ as discussed in Sec. II C.

Amphiphil	k_3 (ϵ)	A_{s0}^*	K_A^*	$A_{s0}(\text{\AA}^2)$	$K_A(\text{mJ m}^{-2})$
ht_4	0	(2.34 ± 0.01)	13.6 ± 1.6	26.0 ± 0.1	408 ± 48
HT_4	2	(2.15 ± 0.02)	11.8 ± 1.5	23.9 ± 0.2	354 ± 45
HT_4	5	(1.83 ± 0.02)	12.2 ± 1.6	20.3 ± 0.2	366 ± 48
$H_3(T_4)_2$	2	(4.16 ± 0.02)	14.3 ± 2.0	46.3 ± 0.2	429 ± 60

per chain for the $H_3(T_4)_2$ surfactant (with two chains) is 3% smaller than for the HT_4 surfactant with the same chain stiffness. This is because the configurations of the two chains in the same $H_3(T_4)_2$ molecule are strongly correlated.

By using the values for ϵ , m , and σ as given in Sec. II C, one can estimate the stretching modulus and the area per surfactant molecule A_0 in physical units, see Table IV. For the $H_3(T_4)_2$ surfactants, the area per surfactant A_s has the value $A_s \approx 46.3 \text{ \AA}^2$, which is smaller than for typical lipids with $A_s \approx 65 \text{ \AA}^2$. However, real lipids have longer chains and this increases the entropic repulsion in the tail region. The values for the compressibility modulus K_A obtained in this way are of the same order as the values observed for real lipid bilayers.

B. Large tension regime

The curves displayed in Figs. 7 and 8 exhibit a sublinear behavior for large areas A_s per surfactant molecule. For the $H_3(T_4)_2$ surfactants, the interfacial tension Σ has been studied for even larger areas A_s , see Fig. 8. If one increases A_s beyond the values shown in Fig. 8 the bilayers exhibit hydrophilic pores. Within 5×10^4 MC steps and 8×10^5 MD steps, no pore formation has been observed for the other less stretched bilayers.

The qualitative behavior of the interfacial tension Σ as a function of the surfactant area A_s can be understood from a rather simple picture as originally envisaged for monolayers.^{23,24} Thus, each monolayer of the bilayer is viewed as a thin film which contains a two-dimensional gas of tail particles. Such a gas should have a free energy per particle or chemical potential μ_s , which becomes large for small A_s . For an ideal gas, for example, one has $\mu_s = -k_B T \ln(A_s/\lambda^2)$ where λ is the de Broglie wavelength. In addition, the free energy of the film has another contribution arising from the interfacial tension Σ_{sw} of the surfactant/water interface. If one combines both terms, one has the free energy f_s per surfactant molecule as given by $f_s \approx \mu_s(A_s) + \Sigma_{sw} A_s \approx -k_B T \ln(A_s/\lambda^2) + \Sigma_{sw} A_s$, where the second estimate holds only for an ideal gas of tails. For interacting tails the first term exhibits a different functional dependence on A_s but it will still increase for small A_s ; for a recent review, see Ref. 25. Furthermore, the interfacial tension Σ_{sw} in the second term increases if one increases the amplitude or the range of the repulsive forces between the water and the tail particles.

The free energy F of the bilayer is then estimated to be $F = N_s f_s$ and the interfacial tension $\Sigma = \partial F / \partial A$ for fixed N_s

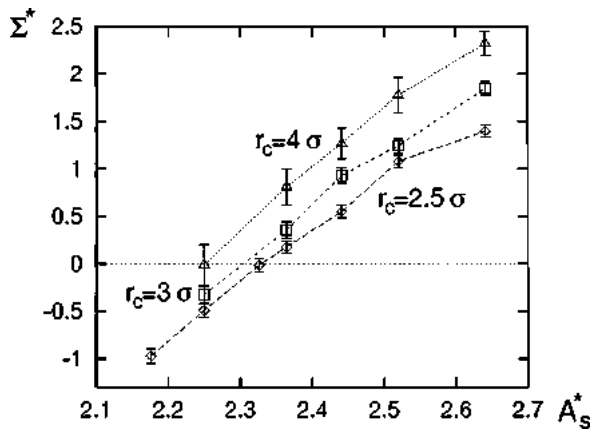


FIG. 9. Dependence of the surface tension Σ^* on the area A_s^* per lipid for flexible ht_4 surfactants with three different cutoffs. For the top curve with the cutoff radius $r_c = 4\sigma$, the behavior is fairly linear over the whole range of A_s^* values.

with the total area $A \equiv N_s A_s / 2$. This implies $\Sigma = 2 \partial f_s / \partial A_s$ which vanishes at $A_s = A_0$ where $f_s(A_s)$ has a minimum and approaches the constant value $2 \Sigma_{sw}$ for large A_s . Therefore, for large A_s the tension exhibits a sublinear behavior as a function of A_s as observed in the simulations.

In Fig. 9, we show the interfacial tension as obtained from simulations using interaction potentials with different cutoff radii r_c as introduced after Eq. (2.2). One finds that the linear regime with $\Sigma \sim A_s - A_0$ increases with increasing r_c . For the largest value $r_c = 4.0\sigma$, the behavior is linear over the whole range of A_s -values.

C. Stress and density profiles

A more detailed description of the state of the bilayer is obtained in terms of the stress profile $s(z)$ as introduced in Eq. (5.6) above. The stress profile for bilayers has been previously discussed by Helfrich²⁶ using heuristic arguments and by Ben Shaul and co-workers²⁵ via mean field theories for the configurations of the surfactant chains.

In the following, we will determine the stress profile via MD simulations. We will explicitly discuss this profile for the case of a tensionless bilayer built up from semiflexible HT_4 surfactants with $k_3 = 2\epsilon$. This bilayer was characterized by the projected surfactant area $A_s = 2.16\sigma^2$ and by the interfacial tension $\Sigma = 0.06\epsilon\sigma^{-2}$. We have also performed simulations for the two other types of model surfactants; the results were found to be similar.

As explained before, the kinetic part of the microscopic stress tensor does not contribute to the stress profile $s(z)$. Thus, it is only the interaction part of the microscopic stress tensor which determines this profile. This interaction part, $\sigma_{in}^{\alpha\beta}$, depends linearly on the gradients $\nabla_i^\alpha \Phi$ of the total potential energy Φ , see Eq. (B1). In the present case, the total potential energy contains contributions from (i) the Lennard-Jones and soft core potentials between the hydrophilic and hydrophobic particles, (ii) the bond potentials U_2 , and (iii) the bending potentials U_3 along the chains. Therefore, each of these potentials gives a contribution to the total stress profile $s(z)$.

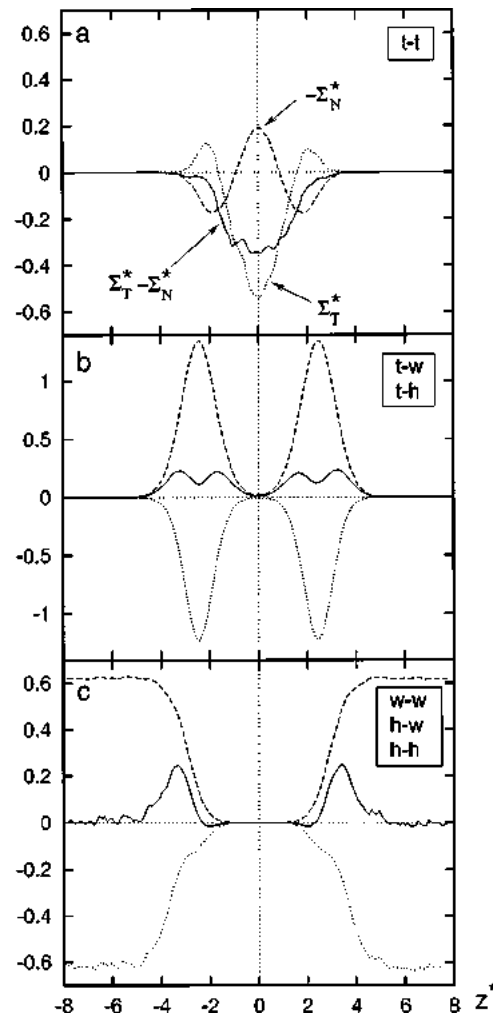


FIG. 10. The stress profile s^* across a bilayer of semiflexible HT_4 surfactants as a function of the coordinate z^* which measures the distance from the midplane of the bilayer along the normal direction. The total stress s^* is equal to $\Sigma_T^* - \Sigma_N^*$ (solid curves), and the tangential and the normal component Σ_T^* and $-\Sigma_N^*$ are given by the dotted and the dashed curves, respectively. (a) Contributions from the Lennard-Jones potential for tail-tail (t-t) interactions; (b) contributions from the soft core potential for tail-water (t-w) and tail-head group (t-h) interactions; and (c) contributions from the Lennard-Jones potential for water-water (w-w), headgroup-water (h-w), and head group-head group (h-h) interactions.

The MD data obtained for these different contributions are displayed in Figs. 10, 11, and 12. In these figures, we show dimensionless stress profiles s^* as functions of the dimensionless coordinate z^* ; the latter coordinate represents the distance from the midplane of the bilayer along the normal direction.

In Fig. 10, the different contributions arising from the Lennard-Jones and the soft core potentials are displayed. In each case, we show the tangential component Σ_T^* , the normal component $-\Sigma_N^*$, and the difference $s^* = \Sigma_T^* - \Sigma_N^*$.

In Fig. 10(a), the contribution arising from the Lennard-Jones potentials between the tail particles is displayed. We see that this contribution is confined to the interior of the bilayer and that it is dominated by a negative tangential component which represents a compression in the direction parallel to the bilayer. This agrees with the intuitive picture that

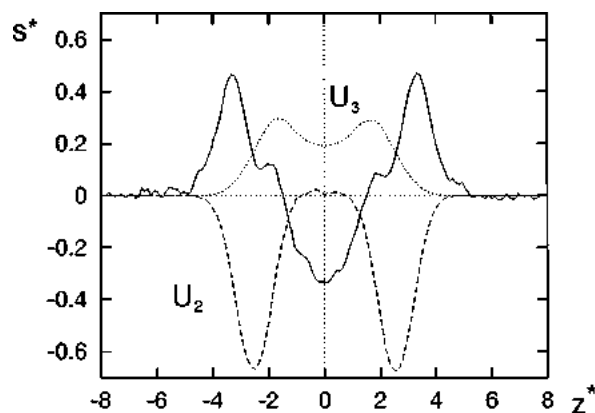


FIG. 11. Different contributions to the stress profile s^* as a function of the distance z^* arising from Lennard-Jones and soft core potentials (solid curve), bond potentials U_2 (dashed curve) and bending potentials U_3 (dotted curve). The solid curve represents the sum of all contributions displayed in Fig. 10.

the tail particles behave as a compressed two-dimensional gas. In Fig. 10(b), we display the stress profile arising from the repulsive soft core potential between the tail and the hydrophilic particles. This leads to a positive contribution to the interfacial tensions between the hydrophobic bilayer interior and the bilayer/water interface. Finally, the contribution from the Lennard-Jones potentials between the hydrophilic particles is shown in Fig. 10(c). The corresponding stress vanishes away from the two surfactant water interfaces and makes a positive contribution to the tension of these interfaces.

Thus, both the repulsive soft core potentials between the tail particles and the hydrophilic particles and the Lennard-Jones potentials between the hydrophilic particles give a contribution to the interfacial tension of the bilayer/water interface. Inspection of Figs. 10(b) and 10(c) shows that these two contributions are comparable in size (note the different units in these two figures).

The stress profile arising from all Lennard-Jones and all soft core potentials is given by the solid curve in Fig. 11. It has the expected behavior: The two bilayer/water interfaces are characterized by positive interfacial tensions whereas the bilayer interior represents a compressed region of tails. In Fig. 11, we also display the stress profiles arising from the bond potentials U_2 and from the bending potentials U_3 . The contribution from the bond potential U_2 is confined to the interfacial regions between the bilayer and the water. This contribution which is large and negative corresponds to normal stretching of the chains by the “anchorage” to the two bilayer/water interfaces. Since the elastic modulus k_2 is rather large in our simulations, even relatively small displacements give large contributions to the stress. The contribution of the bending potential U_3 , on the other hand, is positive which reflects the fact that the tails fluctuate and thus deviate from straight rod configurations.

The total stress profile arising from all interaction potentials is shown in Fig. 12(a). In order to identify the location of the different “layers” of positive and negative stress, the density profiles of the different types of particles are displayed in Fig. 12(b).

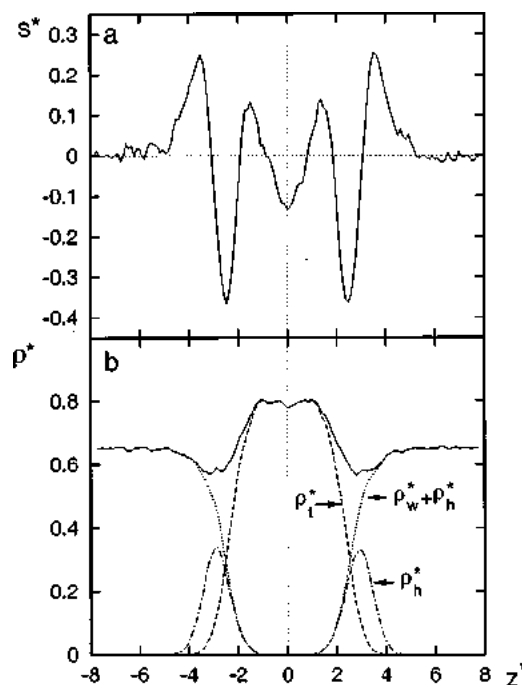


FIG. 12. (a) Total stress profile s^* as a function of the coordinate z^* . This stress profile represents the sum of the curves shown in Fig. 11; (b) density profile ρ^* vs z^* . The solid curve represents the total density. The contributions from the head group, the hydrophilic particles (head groups and water) and the tails are given by the dotted-dashed, dotted, and dashed curves, respectively.

Comparison of the total stress profile in Fig. 12(a) with the different contributions in Figs. 11 and 10 shows that the positive peak of the total stress profile, which is located between the head groups and the water, arises both from the Lennard-Jones and the soft core potentials and represents the interfacial tension which one expects naively. The adjacent region of compression with negative values of $s(z)$, on the other hand, is unexpected and results from the stretching of the bonds along the chain. The large magnitude of this compression reflects the large size of the elastic modulus k_2 . The second positive peak of the total stress profile, which is located at the interface between the head groups and the tails, arises mainly from the bending potential as is evident if one compares the different contributions in Fig. 11. Finally, the negative peak around the midplane of the bilayer corresponds to the compressed tail region as expected.

In summary, we find that all interaction potentials make significant contributions to the total stress profile. In particular, the contributions arising from the bond potentials U_2 and the bending potentials U_3 cannot be neglected compared to the contributions from the Lennard-Jones and the soft core pair potentials but lead to additional negative and positive peaks in the stress profile, respectively. The interfacial tension Σ of the bilayer is given by the integral $\int dz s(z)$. In the present case of an almost tensionless bilayer, this integral is close to zero, which means that the area under the five positive peaks of the stress profile is roughly equal to the area under its three negative peaks. It remains to be seen if this multiple-peak structure of the stress profile $s(z)$ is generic and if the same number of peaks is also present in more realistic models of the water surfactant system.

VII. SUMMARY AND OUTLOOK

In summary, we have shown that the binary Lennard-Jones fluids studied here lead to the formation of micelles and bilayers. The dependence of the type of aggregate on the surfactant concentration is summarized in Table I. The bilayer membranes are in a fluid state which is characterized by rapid lateral diffusion along the membranes. We have measured the corresponding diffusion coefficients of the water and the surfactant particles, see Table III. In addition, we have determined the interfacial tension of the bilayer which is induced by the finite size of the simulation box.

One important aspect of our work is the identification of *tensionless* bilayer states as appropriate for real bilayer membranes which do not experience external constraints. These tensionless states were found by measuring the interfacial tension as a function of the box size and, thus, as a function of the area per surfactant molecule. The derivative of the interfacial tension with respect to the surfactant area determines the area compressibility modulus, see Table IV.

For one such tensionless state, the stress profile was analyzed in detail and it was found that *all* interaction potentials make a significant contribution to this profile. As a result, the stress profile determined above has several maxima and minima which have not been anticipated from heuristic arguments.

In the models studied here, the self-assembly process is driven by the pair interactions between the different types of particles. This mechanism applies directly to systems for which the aggregation process is primarily driven by *enthalpy*. One example is provided by solutions of semifluorinated alkanes in hydrocarbon or fluorocarbon solvents.^{13–16} Our simulations show that these systems can exhibit both micelles and bilayers.

As far as *aqueous* solutions are concerned, the pair interactions used in our models should be regarded as effective, temperature-dependent interactions which incorporate the entropic forces arising from the hydrogen bond networks present in real systems. It remains to be seen if one can find useful relations between these effective interactions and the parameters of microscopically refined models in which the hydrogen bond networks are explicitly simulated. Likewise, it remains to be seen if the qualitative form of the stress profile as found here also applies to such refined models.

As emphasized in Sec. I, the work presented here was performed in order to bridge the gap between bilayer models with (almost) atomic resolution and continuous membrane models. One important parameter which enters in the continuous models is the bending rigidity of the membranes. Recently, we have been able to extract this elastic modulus via additional MD simulations on even larger systems as will be described elsewhere.

ACKNOWLEDGMENTS

We thank Gerhard Gompper for helpful discussions and Gerhard Findenegg for useful remarks on semifluorinated alkanes.

APPENDIX A: TECHNICAL DETAILS

The MD part of the simulations is performed using the LEAP-FROG algorithm²⁷ at constant temperature. The time step is $\Delta t \equiv t_{sc}/2000$ with the time scale $t_{sc} \equiv \sqrt{m\sigma^2/\epsilon}$. The temperature $k_B T = 1.35\epsilon$ is kept constant by rescaling the velocities at every time step. For the MC part, we used the standard METROPOLIS algorithm. One MD time step for a simulation with 1440 particles took 0.3 s on a SGI INDY R4400 (150 MHz). One MC step, i.e., trying every particle once, took about twice that time.

We used three kinds of initial configurations: (i) Randomly distributed surfactant and water molecules. (ii) Preassembled ordered bilayers in which the head group particles are on a two-dimensional lattice with some random in-plane displacements from their lattice positions. The tail particles are added along the normal direction of the lattice, i.e., parallel to the z axis with some small deviations from this orientation. The water molecules were distributed randomly in the remaining space not occupied by the bilayer. (iii) End configurations of previous simulations.

For a randomly chosen initial distribution of the particles, one always finds very small distances between some particles in these configurations. This leads to very large forces acting on these particles which are hard to handle in MD simulations. Therefore, all initial configurations with randomly chosen particle positions were first relaxed via a MC simulation. Since the MC steps are more time consuming than the MD steps, we tried to keep the number of MC steps as small as possible. A convenient choice was between 0.5 and 1.6×10^5 MC steps. These initial MC simulations were followed by long MD simulations consisting of up to 32×10^5 time steps.

For the random initial configuration and the MC simulation, we used the following linear congruential pseudorandom number generator:

$$Y_i = (69069Y_{i-1} + 1) \bmod 2^{32}, \quad (\text{A1})$$

$$\tilde{Y}_i = Y_i / 2^{32}, \quad (\text{A2})$$

where Y_i with $i = 1, 2, \dots$ represents the series of random numbers and \tilde{Y}_i their projection into the interval between 0 and 1. For a careful data analysis, only uncorrelated samples should be used in order to calculate its average values and the standard deviations, which are used to estimate the errors. Therefore we estimate the correlation time by measuring the autocorrelation function $C(\tau)$ of the total interaction potential Φ as defined in Eq. (2.8). This correlation function is given by

$$C(\tau) = \frac{\langle \Phi(t+\tau)\Phi(t) \rangle - \langle \Phi(t) \rangle^2}{\langle \Phi^2(t) \rangle - \langle \Phi(t) \rangle^2}. \quad (\text{A3})$$

The measurement of the autocorrelation function $C(\tau)$ on a run with 3.2×10^6 MD steps shows three correlation times of

140, 650, and about 4000 time steps. As a consequence, we used a sampling time of 5000 time steps for most of our measurements.

APPENDIX B: INTERACTION PART OF THE MICROSCOPIC STRESS TENSOR

We consider a system of classical particles with positions \mathbf{r}_i and momenta \mathbf{p}_i ; the interparticle potentials are taken to be independent of the momenta and translationally invariant but otherwise arbitrary. As shown in Ref. 20, the interaction part of the microscopic stress tensor is then given by

$$\sigma_{\text{in}}^{\alpha\beta} = \sum_i \nabla_i^\alpha \Phi(\{\mathbf{r}_i\}) \int_{\mathcal{C}_{0i}} dl^\beta \delta(\mathbf{R}-\mathbf{l}) \quad (\text{B1})$$

with contours \mathcal{C}_{0i} which connect an arbitrarily chosen position \mathbf{R}_0 with the particle position \mathbf{r}_i .

The total interparticle potential Φ can be divided into two-body, three-body, and more-body potentials which implies

$$\Phi(\{\mathbf{r}_i\}) = \sum_m \Phi^{(m)}(\{\mathbf{r}_i\}) = \sum_m \sum_{\langle j \rangle} U^{(m)}(\mathbf{r}_{j_1}, \dots, \mathbf{r}_{j_m}), \quad (\text{B2})$$

where $U^{(m)}$ denotes the m -body potential. The summation over $\langle j \rangle$ includes all m clusters labeled by $\langle j \rangle = (j_1, j_2, \dots, j_m)$. The contribution to the microscopic stress tensor arising from $\Phi^{(m)}$ is given by

$$[\sigma_{\text{in}}^{\alpha\beta}]^{(m)} = \sum_{\langle j \rangle} \sum_{k=1}^m [\nabla_{j_k}^\alpha U^{(m)}(\mathbf{r}_{j_1}, \mathbf{r}_{j_2}, \dots, \mathbf{r}_{j_m})] \times \int_{\mathcal{C}_{0j_k}} dl^\beta \delta(\mathbf{R}-\mathbf{l}). \quad (\text{B3})$$

Here the particles in the m -cluster $\langle j \rangle$ are labeled by j_1, j_2, \dots, j_m . Now we select one particle in each cluster, say with label j_l , and choose the contours as $\mathcal{C}_{0j_k} = \mathcal{C}_{0j_l} + \mathcal{C}_{j_l j_k}$, i.e., all contours contains the same segment \mathcal{C}_{0j_l} which connects \mathbf{R}_0 with \mathbf{r}_{j_l} . If these contours are inserted into (B3), one obtains two terms. However, the first term arising from the \mathcal{C}_{0j_l} segment vanishes since it is proportional to the sum over all m -body forces $\nabla_{j_k}^\alpha U^{(m)}$ in one cluster and $U^{(m)}$ is taken to be translationally invariant. Therefore, one is left with the second term arising from the $\mathcal{C}_{j_l j_k}$ segments and

$$[\sigma_{\text{in}}^{\alpha\beta}]^{(m)} = \sum_{\langle j \rangle} \sum_{k=1}^m [\nabla_{j_k}^\alpha U^{(m)}(\mathbf{r}_{j_1}, \mathbf{r}_{j_2}, \dots, \mathbf{r}_{j_m})] \times \int_{\mathcal{C}_{j_l j_k}} dl^\beta \delta(\mathbf{R}-\mathbf{l}). \quad (\text{B4})$$

Since there is nothing special about the value of l we average over all possible choices of l . This leads to an expression for which each pair of particles in m -cluster $\langle j \rangle$ occurs twice. Finally, we choose the contour $\mathcal{C}_{j_l j_k}$ to be identical with $\mathcal{C}_{j_k j_l}$ apart from its orientation. In this way, we obtain

$$[\sigma_{\text{in}}^{\alpha\beta}]^{(m)} = \frac{1}{m} \sum_{\langle j \rangle} \sum_{\langle k,l \rangle} (\nabla_{j_k}^\alpha U^{(m)} - \nabla_{j_l}^\alpha U^{(m)}) \int_{\mathcal{C}_{j_l j_k}} dl^\beta \delta(\mathbf{R}-\mathbf{l}), \quad (\text{B5})$$

where the summation over $\langle k,l \rangle$ represents the sum over all possible pairs of particles within a given m cluster.

In order to get a quantity which is accessible to computer simulations, we subdivide the simulation box into thin slices and average the stress tensor over these slices. The slices are perpendicular to the z axis, extend from z_s to $z_s + \Delta z$ and have volume $V_{\Delta z}$. Furthermore, we choose the contours to be linear and parametrize them via

$$l^\beta = r_{j_k}^\beta + \lambda (r_{j_l}^\beta - r_{j_k}^\beta) = r_{j_k}^\beta + \lambda r_{j_k j_l}^\beta. \quad (\text{B6})$$

This choice leads to the averaged microscopic stress tensor

$$[\bar{\sigma}_{\text{in}}^{\alpha\beta}]^{(m)}(z_s) = -\frac{1}{mV_{\Delta z}} \sum_{\langle j \rangle} \sum_{\langle k,l \rangle} \int dX \times \int dY \int_{z_s}^{z_s + \Delta z} dZ (\nabla_{j_k}^\alpha U^{(m)} - \nabla_{j_l}^\alpha U^{(m)}) r_{j_k j_l}^\beta \int_0^1 d\lambda \delta(\mathbf{R} - [\mathbf{r}_{j_k} + \lambda \mathbf{r}_{j_k j_l}]), \quad (\text{B7})$$

where $V_{\Delta z}$ is the volume of the slice. The slice integration can be expressed using Heaviside functions which leads to

$$[\bar{\sigma}_{\text{in}}^{\alpha\beta}]^{(m)}(z_s) = -\frac{1}{mV_{\Delta z}} \sum_{\langle j \rangle} \sum_{\langle k,l \rangle} \int d^3R \theta(Z - z_s) \times \theta(z_s + \Delta z - Z) (\nabla_{j_k}^\alpha U^{(m)} - \nabla_{j_l}^\alpha U^{(m)}) r_{j_l j_k}^\beta \times \int_0^1 d\lambda \delta[\mathbf{R} - (\mathbf{r}_{j_1} + \lambda \mathbf{r}_{j_1 j_2})]. \quad (\text{B8})$$

After integration one finds

$$[\bar{\sigma}_{\text{in}}^{\alpha\beta}]^{(m)}(z_s) = -\frac{1}{mV_{\Delta z}} \sum_{\langle j \rangle} \sum_{\langle k,l \rangle} (\nabla_{j_k}^\alpha U^{(m)} - \nabla_{j_l}^\alpha U^{(m)}) r_{j_k j_l}^\beta f(z_j, z_{j_l}, z_s) \quad (\text{B9})$$

with $f(z_1, z_2, z_s)$ as given by

$$f(z_1, z_2, z_s) \equiv \begin{cases} \theta(z_1 - z_s) \theta(z_s + \Delta z - z_1) & \text{for } z_1 = z_2 \\ \frac{1}{z_2 - z_1} \int_{z_1}^{z_2} d\xi \theta(\xi - z_s) \theta(z_s + \Delta z - \xi) & \text{otherwise,} \end{cases} \quad (\text{B10})$$

where $\theta(z)$ is the Heaviside step function with $\theta(z)=0$ for $z<0$, $\theta(z)=1$ for $z>0$, and $\theta(0)=1/2$. For $z_1=z_2=z$ this implies

$$f(z, z, z_s) = \begin{cases} 1 & \text{for } z_s < z < z_s + \Delta z \\ 1/2 & \text{for } z = z_s \text{ or } z = z_s + \Delta z. \end{cases} \quad (\text{B11})$$

For $z_1 \neq z_2$, on the other hand, the expression (B10) leads to

$$f(z_1, z_2, z_s) = \Delta z / |z_2 - z_1| \quad (\text{B12})$$

if (i) $z_1 \leq z_s$ and $z_2 \geq z_s + \Delta z$ or (ii) $z_2 \leq z_s$ and $z_1 \geq z_s + \Delta z$. If both z_1 and z_2 lie within the Δz slice at $z = z_s$, one has $f(z_1, z_2, z_s) = 1$. Slightly different expressions are obtained if only z_1 or only z_2 lie within the Δz slice. However, in all cases, the function f is approximately equal to the inverse of the number of slices between z_1 and z_2 . The latter approximation has been used in the simulations.

When applied to the two-body case, one obtains the coarse-grained stress tensor

$$\begin{aligned} \bar{\sigma}_2^{\alpha\beta}(z_s) &= -\frac{1}{2V_{\Delta z}} \sum_{\langle j \rangle} (\nabla_{j_1}^\alpha U^{(2)} \\ &\quad - \nabla_{j_2}^\alpha U^{(2)}) r_{j_1 j_2}^\beta f(z_{j_1}, z_{j_2}, z_s) \\ &= \frac{1}{V_{\Delta z}} \sum_{\langle j \rangle} (\nabla_{j_1 j_2}^\alpha U^{(2)}) r_{j_1 j_2}^\beta f(z_{j_1}, z_{j_2}, z_s) \end{aligned} \quad (\text{B13})$$

for the contribution from the two-body potential $U^{(2)}$. In this case, the summation over $\langle j \rangle$ includes all possible pairs of particles. Likewise, the coarse-grained stress tensor arising from the three-body potential $U^{(3)}$ is given by

$$\begin{aligned} \bar{\sigma}_3^{\alpha\beta}(z_s) &= -\frac{1}{3V_{\Delta z}} \sum_{\langle j \rangle} \sum_{\langle k, l \rangle} (\nabla_{j_k}^\alpha U^{(3)} \\ &\quad - \nabla_{j_l}^\alpha U^{(3)}) r_{j_k j_l}^\beta f(z_{j_k}, z_{j_l}, z_s), \end{aligned} \quad (\text{B14})$$

where the summation over $\langle j \rangle$ includes all possible triplets and the summation over $\langle k, l \rangle$ represents three terms corresponding to the three possible particle pairs within a given particle triplet.

¹ *Structure and Dynamics of Membranes*, Handbook of Biological Physics Vol. 1, edited by R. Lipowsky and E. Sackmann (Elsevier, Amsterdam 1995).

² E. Egberts and H. J. C. Berendsen, *J. Chem. Phys.* **89**, 3718 (1988).

³ H. E. Alper, D. Bassolino, and T. R. Stouch, *J. Chem. Phys.* **98**, 9798 (1993).

⁴ H. Heller, M. Schaefer, and K. Schulten, *J. Phys. Chem.* **97**, 8343 (1993).

⁵ For a review, see R. W. Pastor, *Curr. Opin. Struct. Biol.* **4**, 486 (1994).

⁶ B. Widom, *J. Chem. Phys.* **81**, 1030 (1984).

⁷ C. Borzi, R. Lipowsky, and B. Widom, *J. Chem. Soc., Faraday Trans. 2* **82**, 1739 (1986).

⁸ M. M. Telo da Gama and K. E. Gubbins, *Mol. Phys.* **59**, 227 (1986).

⁹ B. Smit, P. A. J. Hilbers, K. Esselink, L. A. M. Rupert, N. M. van Os, and A. G. Schlijper, *J. Chem. Phys.* **95**, 6361 (1991).

¹⁰ G. Gompper and M. Schick, in *Phase Transition and Critical Phenomena*, edited by C. Domb and J. Lebowitz (Academic, London, 1994), Vol. 16.

¹¹ A. T. Bernardes, *J. Phys. II* **6**, 196 (1996).

¹² C. Tanford, *The Hydrophobic Effect: Formation of Micelles and Biological Membranes* (Wiley, New York, 1980).

¹³ J. Höpken, C. Pugh, W. Richtering, and M. Möller, *Makromol. Chem.* **189**, 911 (1988).

¹⁴ Y. Hayami and G. H. Findenegg, *Langmuir* **13**, 4865 (1997).

¹⁵ M. P. Turberg and J. E. Brady, *J. Am. Chem. Soc.* **110**, 7797 (1988).

¹⁶ P. Lo Nostro and S. H. Chen, *J. Phys. Chem.* **97**, 6535 (1993).

¹⁷ M. Doi and S. F. Edwards, *The Theory of Polymer Dynamics* (Clarendon, Oxford, 1986).

¹⁸ R. Goetz, Ph.D. thesis, University of Potsdam, Germany, 1997.

¹⁹ J. S. Rowlinson and B. Widom, *Molecular Theory of Capillarity* (Clarendon, Oxford, 1982).

²⁰ O. Schofield and J. R. Henderson, *Proc. R. Soc. London, Ser. A* **379**, 231 (1982).

²¹ J. H. Irving and J. G. Kirkwood, *J. Chem. Phys.* **18**, 817 (1950).

²² S. E. Feller, Y. Zhang, and R. W. Pastor, *J. Chem. Phys.* **103**, 10267 (1995).

²³ G. L. Gaines, *Insoluble Monolayers at Liquid-Gas Interfaces* (Wiley, New York, 1966).

²⁴ P. G. de Gennes and C. Taupin, *J. Phys. Chem.* **86**, 2294 (1982).

²⁵ A. Ben-Shaul, in *The Structure and Dynamics of Membranes*, edited by R. Lipowsky and E. Sackmann (Elsevier, Amsterdam, 1995).

²⁶ W. Helfrich, in *Physics of Defects*, edited by R. Balian *et al.* (North-Holland, Amsterdam, 1981).

²⁷ M. P. Allen and D. J. Tildesley, *Computer Simulations of Liquids* (Oxford, Oxford, 1987).